iScience

Article

Dual NIR-II fluorescence and ratiometric photoacoustic imaging-guided metal-phenolic nanosheets for H_2S-activatable synergistic therapy

Graphical abstract

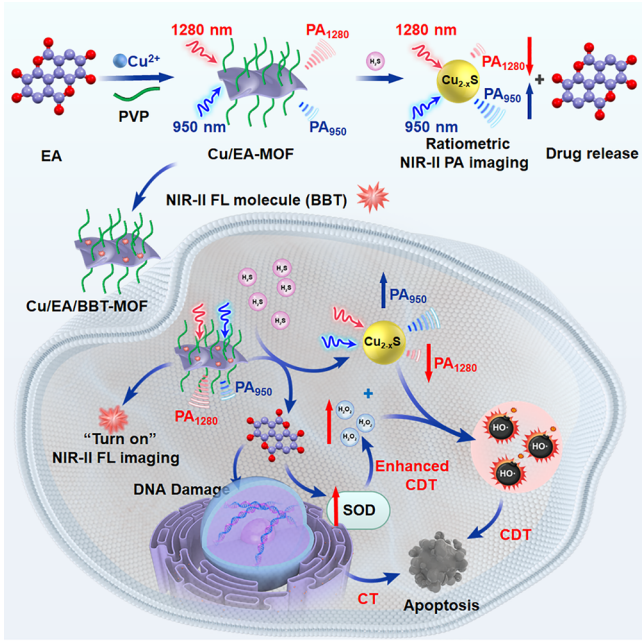

Highlights

- H_2S-triggered NIR-II FL and ratiometric PA imaging nanomaterials were constructed
- Metal-phenolic nanosheets were used for synergistic therapy of colon cancer
- Therapeutic effects were accurately predicted by ratiometric NIR-II PA imaging

Authors

Wenhui Zhang, Min Zhao, Leqiang Wang, ..., Bin Chen, Shi Gao, Jingbin Lu

Correspondence

gaoshi@jlu.edu.cn (S.G.), ljb@jlu.edu.cn (J.L.)

In brief

Health sciences; Chemistry; Materials science

Zhang et al., 2025, iScience *28*, 112425
May 16, 2025
https://doi.org/10.1016/j.isci.2025.112425

CellPress

iScience

CellPress
OPEN ACCESS

Article

Dual NIR-II fluorescence and ratiometric photoacoustic imaging-guided metal-phenolic nanosheets for H_2S-activatable synergistic therapy

Wenhui Zhang,[1] Min Zhao,[2] Leqiang Wang,[1] Jiaqi Wang,[1] Xiaoguang Ge,[2,3] Junzhi Liu,[2] Bin Chen,[2] Shi Gao,[2,4,*] and Jingbin Lu[1,*]

[1]College of Physics, Jilin University, 2699 Qianjin Street, Gaoxin District, Changchun 130012, P.R. China
[2]Departments of Nuclear Medicine China-Japan Union Hospital of Jilin University, Changchun, Jilin 130033, P.R. China
[3]MOE Key Laboratory for Analytical Science of Food Safety and Biology, College of Chemistry, Fuzhou University, Fuzhou 350108, China
[4]Lead contact
*Correspondence: gaoshi@jlu.edu.cn (S.G.), ljb@jlu.edu.cn (J.L.)
https://doi.org/10.1016/j.isci.2025.112425

SUMMARY

Metal-organic frameworks (MOFs) based on nanomaterials have attracted attention for tumor microenvironment (TME)-responsive therapy. However, they lack intrinsic imaging capabilities to monitor drug release and predict therapeutic outcomes. Herein, metal-phenolic nanosheets (Cu/EA-MOF) with photoacoustic (PA) imaging property in the second near-infrared window were constructed to achieve diagnosis and treatment for H_2S-enriched tumors. Endogenous H_2S triggers the decomposition of Cu/EA-MOF into the ellagic acid (EA) and copper sulfide ($Cu_{2-x}S$), which can be used for chemotherapy and chemodynamic therapy, respectively. Moreover, EA can enhance the efficiency of chemodynamic therapy by boosting superoxide dismutase activity. Importantly, the degradation of Cu/EA-MOF can be indicated via the change of ratiometric PA signal intensity. Furthermore, the NIR-II fluorescent molecule benzobisthiadiazole (BBT) was further introduced into Cu/EA-MOF to investigate the degradation process and drug release. As a promising theranostic nanomaterial, Cu/EA/BBT-MOF is successfully used to achieve effective synergistic therapy and predict therapeutic outcomes.

INTRODUCTION

The development of stimuli-responsive theranostic agents is an emerging trend in cancer diagnosis and treatment.[1–3] Consequently, many drug delivery systems with stimulus-responsive drug release have been reported.[4–7] Stimuli-responsive metal-organic frameworks (MOFs) represent an ideal and prospective class of nanomaterials for drug delivery owing to the abundance and availability of their metal ions and ligands, both of which can be harnessed for cancer therapy and bioimaging applications.[8] Nevertheless, the traditional methods of loading drugs into MOFs involve encapsulating drugs via multiple interactions, such as electrostatic interaction, hydrogen bonding, coordination, and π-π stacking.[9,10] Drugs without specific functional groups may have compromised by low loading efficiency and poor stability within MOFs. Employing both functional linkers with intrinsic antitumor activities and active ions to fabricate MOFs would improve the loading efficiency of drugs and prevent the additional introduction of drugs with safety concerns.[11,12] Moreover, this strategy can effectively enhance the therapeutic efficacy via synergistic effects of ions and linkers.

Natural bioactive polyphenols, as candidate substitutes for conventional chemotherapy drugs, contain many phenolic hydroxyl groups, which can coordinate with metal ions to form MOFs.[13–17] They show high potential in the field of antitumor, benefiting from their excellent biosafety and stimulus-responsive ability in the tumor microenvironment (TME).[18–21] Realizing the controllable release of drugs is highly desired, as it is conducive to achieving individual and precise therapy.[22–24] The real-time monitoring of drug release in the tumor is essential to predict therapeutic efficacy.[25–27] Although many kinds of MOFs with excellent antitumor effects have been constructed, the lack of precise imaging tools during therapy made a challenge for their bioapplications.

Recently, the biomedical applications of photoacoustic (PA) and fluorescence (FL) imaging in the second near-infrared window (NIR-II, 900–1700 nm) have attracted widespread attention due to their deep tissue penetration, high resolution, and low background signal interference.[28–32] Single-mode imaging frequently fails to supply comprehensive information essential for the precise diagnosis and treatment of cancer. The combination of NIR-II FL and PA imaging compensates for their inherent limitations, thus, providing accurate and abundant information and enhancing the accuracy of cancer diagnosis for each imaging modality.[33] Consequently, the rational design and fabrication of NIR-II FL/NIR-II PA dual-modal imaging-guided multimodal comprehensive cancer therapies effectively meet the urgent requirements for accurate cancer diagnosis and precise, effective treatment.

Limited by the light scattering and the change of probe concentration in biological tissues, single intensity-dependent signal of PA imaging is fluctuant and distorted. However, these limitations can be circumvented by constructing a self-calibration signal.[34–36] The ratiometric NIR-II PA imaging has the great potential in understanding therapeutical process due to its ability to precisely monitor the intensity ratio of two or more signal channels. However, to our knowledge, nanoMOFs with the intrinsic ability of NIR-II PA imaging *in vivo* have not been reported. Therefore, the construction of MOFs with the ability to facilitate stimuli-responsive ratiometric NIR-II PA imaging will significantly contribute to the development of individual and precise cancer therapies.

In this study, stimuli-responsive MOF nanosheets containing Cu^{2+} and ellagic acid (EA), designated as Cu/EA-MOF, were developed to achieve synergistic combination therapy consisting of both chemotherapy and enhanced chemodynamic therapy (CDT), guided by ratiometric NIR-II PA imaging (Figure 1A). In order to better visualize distribution and destruction of Cu/EA-MOF, NIR-II fluorescence molecule (BBT) was introduced into Cu/EA-MOF, termed as Cu/EA/BBT-MOF. Upon internalization of Cu/EA/BBT-MOF into the tumor, endogenous hydrogen sulfide (H_2S) induces the decomposition of Cu/EA/BBT-MOF, resulting in the generation of copper sulfide ($Cu_{2-x}S$) and the release of EA, (Figure 1B). $Cu_{2-x}S$ not only serves as an NIR-II PA probe but also triggers a Fenton-like reaction upon exposure to endogenous H_2O_2 *in situ*, generating a cytotoxic hydroxyl radical (•OH) and further inducing tumor cell apoptosis. In addition to possessing chemotherapeutic effects, EA also improves the therapeutic outcome of CDT by enhancing superoxide dismutase (SOD) activity. The presence of EA can promote the generation of H_2O_2 in the tumor tissue, thereby improving the therapeutic outcome. Notably, Cu/EA/BBT-MOF exhibited strong absorption at 1280 nm, while $Cu_{2-x}S$ formed via *in situ* sulfurization of Cu/EA/BBT-MOF and endogenous H_2S exhibited strong absorption at 950 nm. Consequently, the variations in the ratiometric NIR-II PA signal (PA_{950}/PA_{1280}) can monitor the EA release and $Cu_{2-x}S$ generation as a result of the degradation of Cu/EA/BBT-MOF, which can be utilized for early prediction of the synergistic therapy effect. Both *in vitro* and *in vivo* experiments have demonstrated that H_2S-triggered synergistic therapy has excellent antitumor effects, which was successfully predicted by ratiometric NIR-II PA imaging.

RESULTS

Preparation and characterization of Cu/EA-MOF

The process for preparing H_2S-responsive Cu/EA-MOF is illustrated in Figure 2A. EA, a representative natural polyphenol present in various herbs, was selected due to its rigid structure and potential anti-tumor effects.[37,38] Polyvinyl pyrrolidone (PVP)-modified MOF was generated by a one-step hydrothermal method using Cu^{2+} as metal ions and EA as a bridging ligand. The resultant Cu/EA-MOF was further characterized by various techniques. As shown in Figure 2B, the transmission electron microscopy (TEM) image clearly illustrated the 2D nanosheet morphology of Cu/EA-MOF, and the lateral size of the Cu/EA-MOF nanosheets was determined to be 100–180 nm. Energy-dispersive X-ray (EDX) elemental mapping revealed that Cu, N, and O were homogeneously distributed across the entire nanosheet (Figures 2C and S1). X-ray diffraction (XRD) data showed that the reflection peaks of Cu/EA-MOF were well matched to the simulated pattern of MIL-53 frameworks (Cambridge crystallographic data no. CCDC-220475) (Figure 2D), indicating that Cu/EA-MOF formed the MOF structure through coordination between EA and Cu^{2+}.[13] Atomic force microscopy (AFM) revealed that the thickness of the prepared Cu/EA-MOF nanosheets was around 4.25 nm (Figure 2E and 2F). Dynamic light scattering (DLS) data indicated that the average size of Cu/EA-MOF was approximately 200 nm (Figure 2G), which was inconsistent with the size measured by TEM because of the hydration of the nanoparticles. Subsequently, the negligible changes of hydrodynamic diameters in PBS and DMEM confirmed that Cu/EA-MOF exhibited high stability under physiological conditions owing to highly negatively charged (Figures 2H, S2, and S3). This property is beneficial for long-term storage.

The absorption spectrum of the Cu/EA-MOF nanosheets was measured using an ultraviolet-visible-near-infrared (UV-vis-NIR) absorption spectrophotometer (Figure 2I). The absorption spectrum of Cu/EA-MOF was significantly different from those of EA and $Cu(NO_3)_2$, confirming the successful preparation of Cu/EA-MOF. It was also observed that the absorption spectrum of Cu/EA-MOF was mainly located in the NIR-II region with the peak at 1280 nm, suggesting enhanced deep tissue penetration due to reduced light scattering and absorption in biological tissues. Spherical metal-phenolic nanoparticles based on EA-coordinated Cu have been reported, which presented the characteristic peak in the ultraviolet and visible region.[39] Therefore, we speculated that the nanosheet structure was responsible for NIR-II absorption ability of Cu/EA-MOF. In addition, a peak at 550 nm was assigned to the characteristic ligand-to-metal charge transfer band. The emergence of strong NIR-II absorption encouraged us to investigate the NIR-II PA imaging property of Cu/EA-MOF. Furthermore, the PA signals of Cu/EA-MOF at different wavelengths were recorded (Figure 2J). The PA spectrum was closely consistent with the absorption spectrum, implying that the NIR-II PA signal originated from the absorption. The PA signal intensity at 1280 nm was linearly correlated with the concentrations of Cu/EA-MOF (Figure S4). Therefore, Cu/EA-MOF with inherent NIR-II PA imaging ability has great promise for image-guided therapy.

H_2S-responsivity of Cu/EA-MOF *in vitro*

Subsequently, the responsivity of the Cu/EA-MOF to H_2S was investigated *in vitro* (Figure 3A). H_2S, as an endogenous gasotransmitter, is closely associated with tumor growth and proliferation in colon cancer with concentration range of 0.3–3.4 mmol L^{-1}.[40–42] The concentration range of H_2S that produces physiological effects in normal tissues is 10–300 μM.[43] NaHS was chosen as an H_2S donor in *in vitro* experiments, which can generate H_2S in water.[44] Following incubation with NaHS, Cu/EA-MOF was rapidly converted into small nanoparticles with an average size of approximately 8 nm (Figure 3B and 3C). The XRD analyses suggested that the generated nanoparticles were copper sulfide crystals (Cu_9S_8, JCPDS card no. 36-0379) (Figure 3D). The broad and diffuse XRD diffraction peaks were attributed to

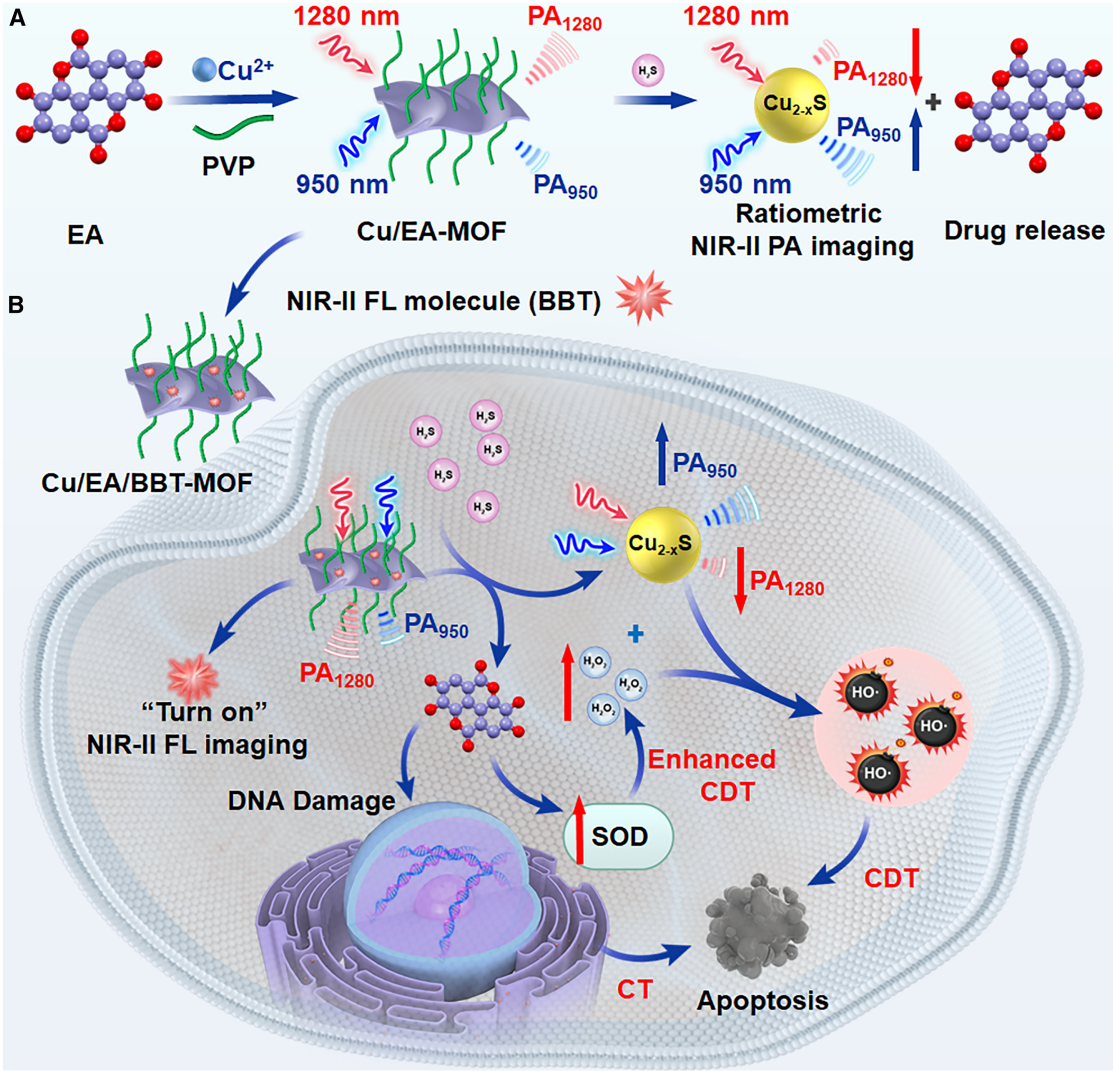

Figure 1. Schematic illustration of preparation and synergistic therapy based on metal-phenolic nanosheets

(A) Schematic illustration of Cu/EA-MOF preparation and its capability for H_2S-triggered ratiometric NIR-II PA imaging.

(B) Mechanistic diagram of how Cu/EA/BBT-MOF facilitates the synergistic combination of chemotherapy and chemodynamic therapy in tumors, guided by NIR-II FL and ratiometric PA imaging.

the polymer. The result of XPS indicated that the valence state of Cu in $Cu_{2-x}S$ was between +1 and +2 (Figure S5). As displayed in Figure 3E, the optical absorption of Cu/EA-MOF gradually increased at 950 nm and decreased at 1280 nm with the increasing concentration of NaHS, which was attributed to the generation of $Cu_{2-x}S$ and the decomposition of Cu/EA-MOF. $Cu_{2-x}S$ had high absorption in the NIR region due to the localized surface plasmon resonance (LSPR) effect.[24] Additionally, we obtained NIR-II PA images at 950 nm and 1280 nm in the presence of different concentrations of NaHS (Figure 3F). This apparent change in NIR-II PA signal intensity can be validated by the change of representative PA spectra (Figure S6). Although the maximum PA signal of Cu/EA-MOF treated with NaHS was around 800 nm located in NIR-I in Figure S6, we investigate the change of NIR-II PA signal at 950 nm in the NIR-II region due to its deeper tissue penetration. As depicted in Figure 3G, the ratio of PA signal intensity at 950 nm and 1280 nm increased linearly with the concentration of NaHS across a broad range (0–3 mM), indicating great potential for quantitative imaging. To evaluate the reaction selectivity of Cu/EA-MOF for NaHS, various interfering species were chosen, which widely were in the living body. The Cu/EA-MOF demonstrated good selectivity for NaHS, and no obvious change in ratiometric intensity was observed during the treatment with other species (Figure 3H). These results proved that the H_2S-responsive decomposition of Cu/EA-MOF can be monitored by ratiometric NIR-II PA imaging.

According to the aforementioned findings, the time-dependent drug release of Cu/EA-MOF was further investigated. Cu/EA-MOF was dispersed in PBS with pH of 7.4 and treated with

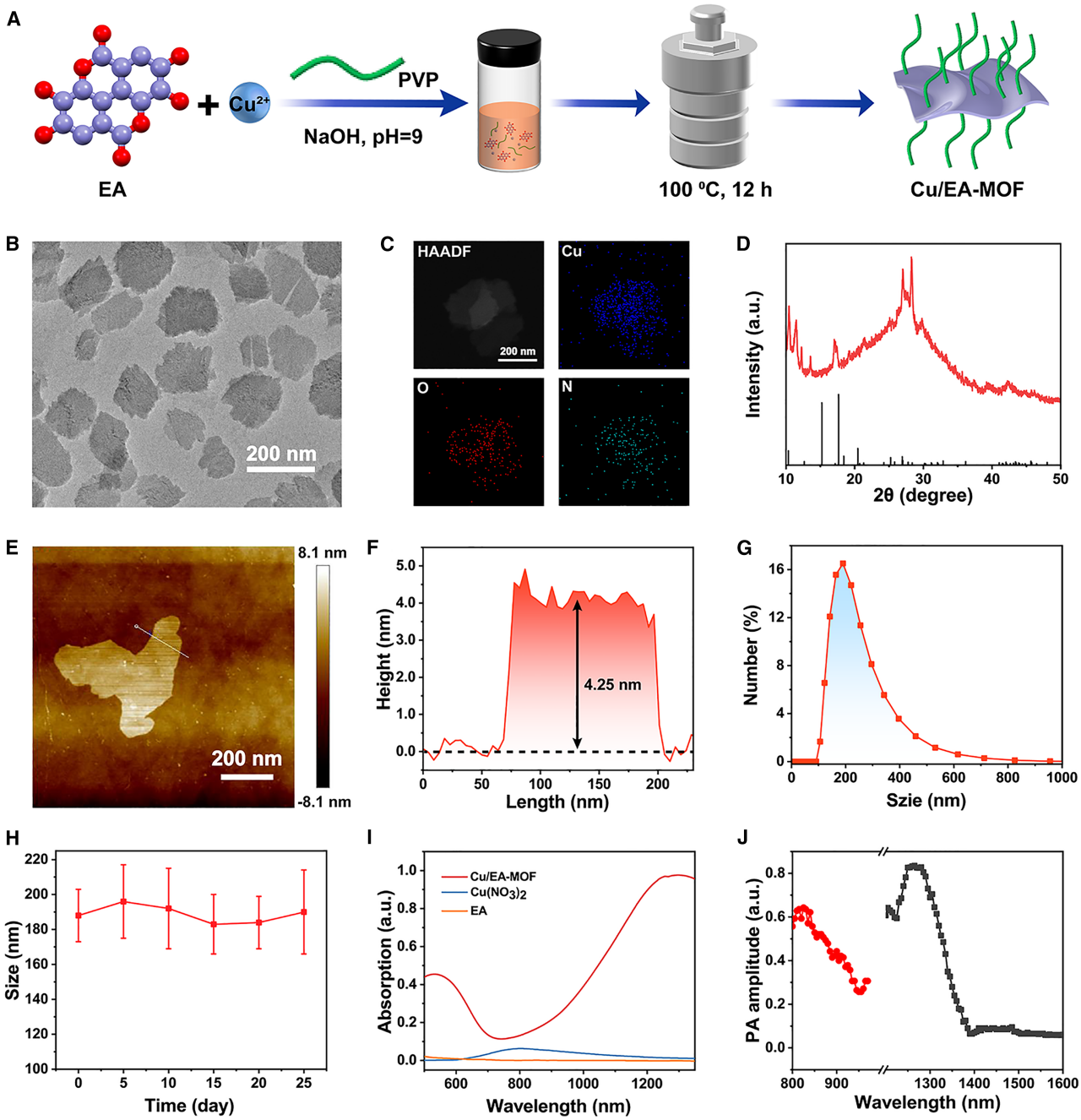

Figure 2. Preparation and characterization of Cu/EA-MOF

(A) Scheme for the preparation of Cu/EA-MOF.
(B) TEM imaging of Cu/EA-MOF.
(C) Corresponding EDS mapping.
(D) XRD spectrum of Cu/EA-MOF.
(E and F) (E) AFM imaging of Cu/EA-MOF (F) the corresponding height profile along the white line in (E).
(G) Size distribution of Cu/EA-MOF.
(H) Stability of Cu/EA-MOF in PBS, pH = 7.4 (n = 3).
(I) Vis-NIR absorption spectra of Cu^{2+}, EA, and Cu/EA-MOF.
(J) PA spectra of Cu/EA-MOF. Data are shown as means ± SD.

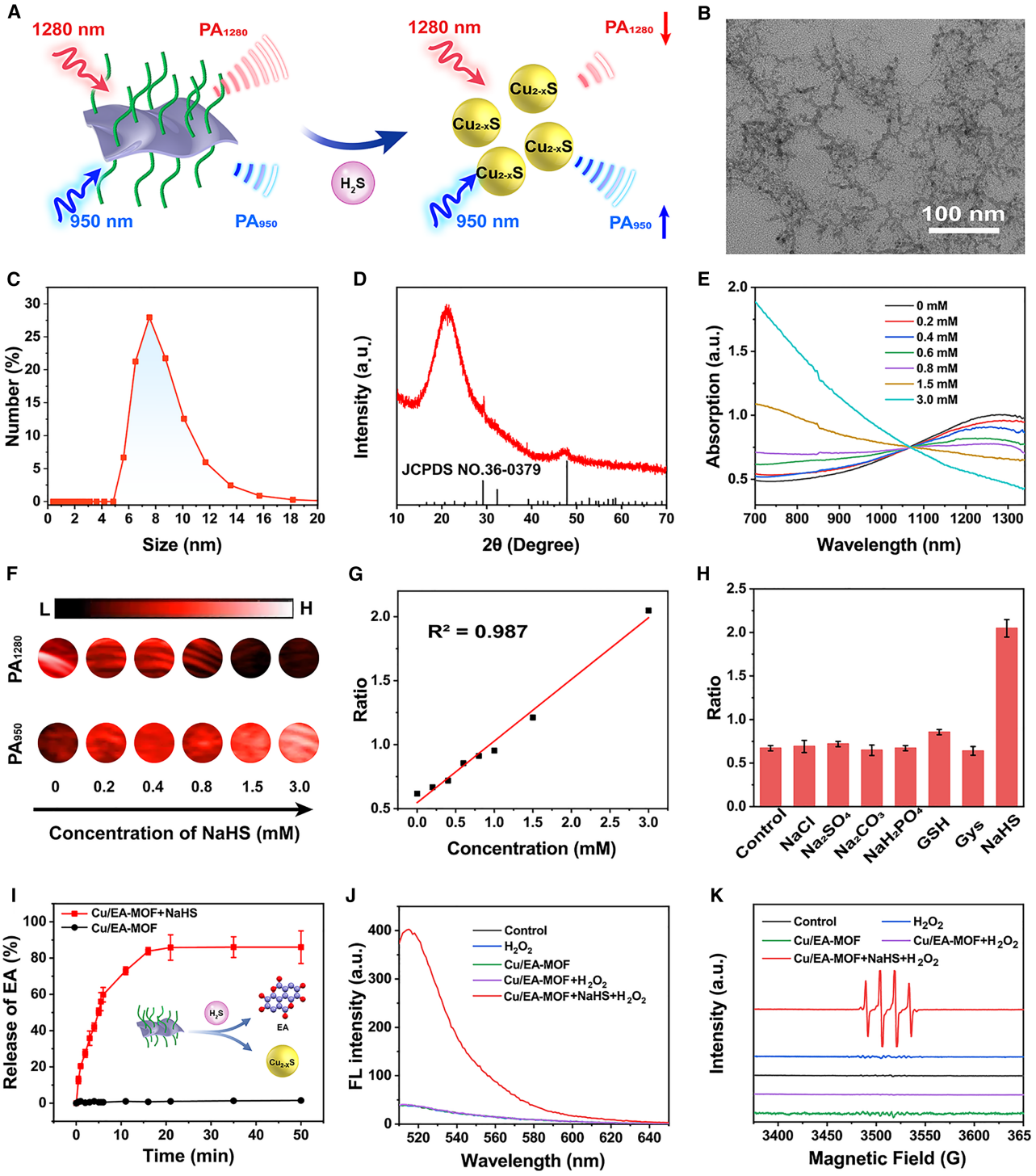

Figure 3. Ratiometric responsivity of Cu/EA-MOF to NaHS

(A) Schematic illustration of the reaction between Cu/EA-MOF and NaHS to produce copper sulfide nanoparticles.

(B) TEM imaging of copper sulfide nanoparticles.

(C) Size distribution of Cu/EA-MOF after reaction with NaHS.

(D) XRD pattern of the $Cu_{2-x}S$ nanoparticles.

(E) Absorption spectra of Cu/EA-MOF after addition with NaHS from 0 to 3.0 mM

(F) PA imaging of the ratiometric response of Cu/EA-MOF to different concentrations of NaHS.

(legend continued on next page)

or without NaHS. As shown in Figure 3I, without incubation of NaHS, EA release was negligible, avoiding non-specific degradation in the normal physiological environment. When Cu/EA-MOF was incubated with NaHS, the release ratio of EA increased to 87% within 20 min, verifying that Cu/EA-MOF possessed H_2S-triggered rapid release behavior. Meanwhile, the release efficiency can be indicated by ratiometric NIR-II PA imaging. Hence, Cu/EA-MOF is capable of highly efficient drug release and $Cu_{2-x}S$ generation in H_2S-enriched cancer microenvironment that can be precisely monitored by accurate imaging.

In addition, $Cu_{2-x}S$ is known to induce the generation of·OH in the presence of H_2O_2 through Fenton-like reactions, achieving oxidative stress-induced cancer therapy.[44] Neither H_2O_2 alone nor Cu/EA-MOF without H_2O_2 enhance FL intensity, which was indicated by the use of hydroxyphenyl fluorescein (HPF) as an ·OH "turn on" specific fluorescent tracer. The FL signal recovery of HPF confirmed the·OH production ability of $Cu_{2-x}S$ (Figure 3J). In addition, the fluorescence signal intensity of HPF increased with increasing concentrations of H_2O_2, suggesting that the H_2S triggered Cu/EA-MOF-mediated Fenton-like reaction was dependent on H_2O_2 concentration (Figure S7A). The FL signal intensity at pH 5.0, 6.5, and 7.4 was negligible, which was beneficial for high efficiency of CDT in the TME (Figure S7B). As shown in Figure S8, the FL intensity of HPF progressively strengthened and finally reached its maximum after 90 min with the increase of time. As displayed in the electron spin resonance (ESR) spectra, the characteristic 1:2:2:1 signal was observed when Cu/EA-MOF, NaHS, and H_2O_2 co-existed in the environment, while no significant signal appeared in the other groups (Figure 3K). These results demonstrated that upon sulfidation, the Cu/EA-MOF performed the conspicuous ability of reactive oxygen species (ROS) generation, which enabled Cu/EA-MOF to trigger CDT for H_2S-enriched tumors.

In vitro synergistic therapeutic effect of Cu/EA-MOF

The prominent H_2S-triggered "turn on" performances of Cu/EA-MOF encouraged us to explore the anticancer effect *in vitro* (Figure 4A). Accumulating evidence has confirmed that tumor-derived H_2S as a signaling molecule plays an important role in many pathological and biological processes, particularly in the development and metastasis of colorectal tumors.[45] In particular, the high concentration of endogenous H_2S has been measured in colon cancer. Accordingly, the mouse colon cancer cells (MC38) line was selected to investigate the therapeutic efficacy. MC38 cells were pretreated with SAM to regulate the level of endogenous H_2S, which is a promoter for endogenous H_2S biosynthesis.[46] $ZnCl_2$ was employed to scavenge endogenous H_2S. Firstly, the cytocompatibility was assessed on human normal liver cells (L02) by cell counting kit-8 assay. As shown in Figure 4B, the cell viability of L02 cells was higher than 90% after incubation with different concentrations of Cu/EA-MOF, implying the excellent biocompatibility in healthy tissues. Notably, Cu/EA-MOF presented serious cell lethality for MC38 cells, indicating the specific therapy for colorectal tumor cells without causing damage to normal cells (Figure 4C). The cell viability of MC38 treated with Cu/EA-MOF was higher than those treated with Cu/EA-MOF+SAM, originating from the relatively low level of H_2S in MC38 cells *in vitro* without treated with SAM (Figure S9). To further tap into the H_2S-triggered therapeutic effect of Cu/EA-MOF, MC38 cells were pre-treated with either SAM or $ZnCl_2$. The Cu/EA-MOF had a high cytotoxicity toward the MC38 cells pretreated with SAM, while no obvious cytotoxicity was observed in Cu/EA-MOF + $ZnCl_2$ group (Figure 4D). The flow cytometry results further revealed that both control group and the Cu/EA-MOF + $ZnCl_2$ group performed no obvious signs of apoptosis (Figure 4E). However, the MC38 cells showed significant signs of apoptosis in Cu/EA-MOF + SAM group. In addition, EA alone can lead to signs of apoptosis in MC38 cell, validating its chemotherapeutic effect. The investigation of live (green) and dead (red) staining assay visually confirmed the aforementioned results (Figure S10). Colony formation assay manifested that Cu/EA-MOF presented excellent suppressing angiogenesis effect (Figures 4F and S11). All aforementioned findings indicated the effectiveness of H_2S-triggered synergistic therapy.

The synergistic therapy mechanism

Having manifested the *in vitro* promising therapeutic effect of Cu/EA-MOF, we further investigated its working mechanisms. Firstly, the *in vitro* $Cu_{2-x}S$ generation and EA release were explored by NIR-II FL and PA imaging. NIR-II organic fluorophores based on donor-acceptor-donor have been applied for bioimaging due to their excellent imaging performance under physiological conditions. A NIR-II FL imaging molecule derived from a benzobisthiadiazole (BBT) core with triphenyl amine that we synthesized in previous study.[47] The chemical formula of BBT is shown in Figure S12. In order to better visualize destruction of Cu/EA-MOF, NIR-II FL molecule (BBT) was introduced into Cu/EA-MOF, termed as Cu/EA/BBT-MOF (Figure 5A). As shown in Figure 5B, the typical absorbance peak of BBT at around 700 nm could be observed in Cu/EA/BBT-MOF, which evident the presence of BBT in nanoparticles. The quenching and recovery efficacies of FL were 80.9% and 85.5%, respectively (Figure S13A). The Cu/EA/BBT-MOF showed the good selectivity for NaHS, and no obvious change in FL intensity was observed during the treatment with other species (Figure S13B). Cu/EA-MOF is a good photoinduced electron transfer quencher, leading to low NIR-II FL signal intensity of Cu/EA/BBT-MOF. Additionally, upon the addition of NaHS, the dose-dependent increase of NIR-II FL signal intensity at 1050 nm excited by 808 nm laser was confirmed (Figure 5C). In the stability experiment of Cu/EA/BBT-MOF, the low signal of fluorescence in solution indicated that there was no BBT leakage from Cu/EA/BBT-MOF, which was due to the strong

(G) Linear correlation between the ratio of PA intensity (PA_{950}/PA_{1280}) and the corresponding concentration of NaHS.
(H) PA ratio (PA_{950}/PA_{1280}) of Cu/EA-MOF treated with interfering species for 2 min
(I) Time-dependent release of EA from Cu/EA-MOF treated with or without 1 mM NaHS.
(J) Generation of •OH determined using hydroxyphenyl fluorescein (HPF) as a probe.
(K) ESR spectroscopy of •OH generation by different groups. H_2O_2 concentration in (J) and (K) was 5 mM. Data are shown as means ± SD.

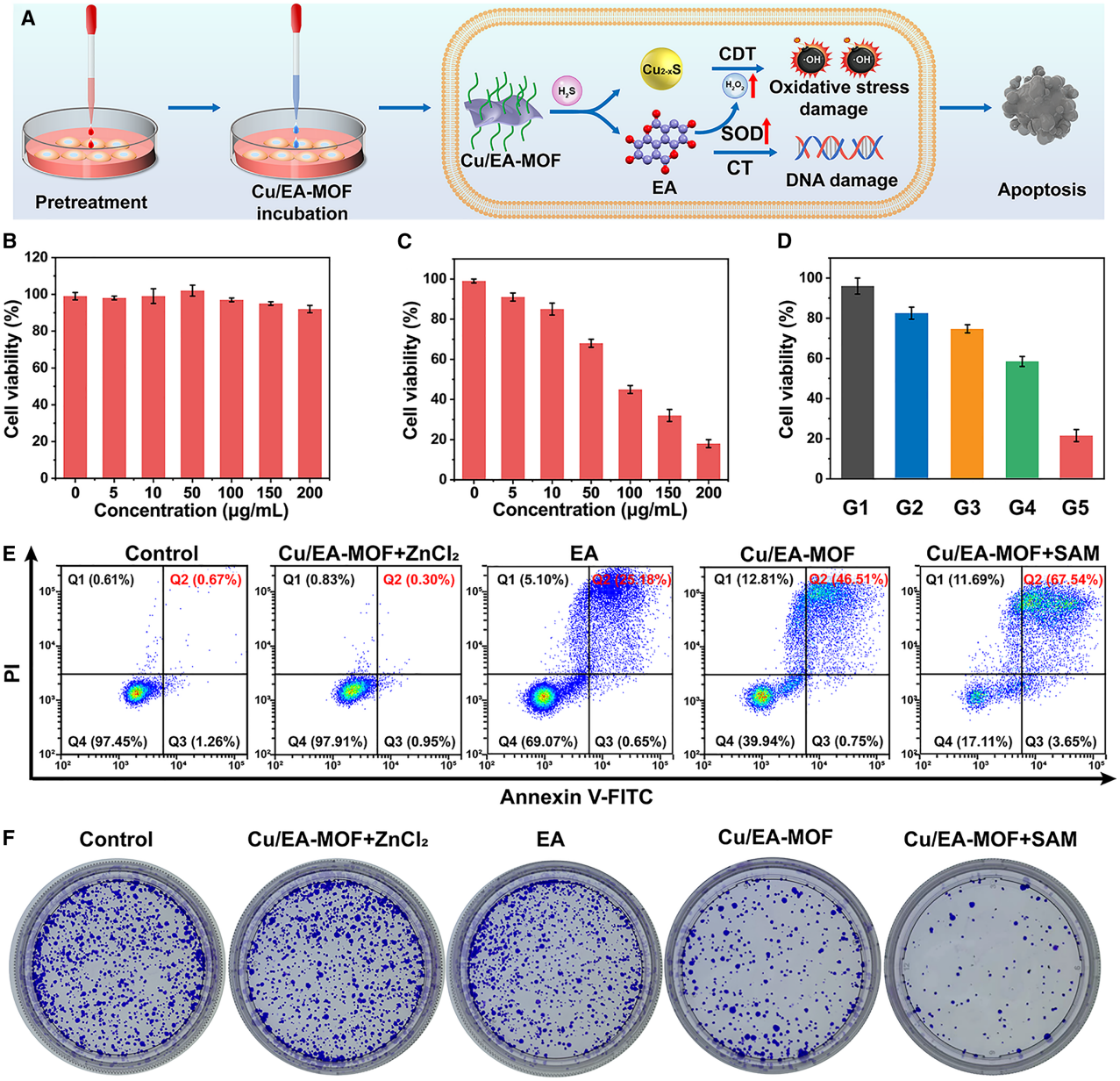

Figure 4. *In vitro* synergistic therapeutic effect of Cu/EA-MOF

(A) Schematic illustration of synergistic therapy effect of Cu/EA-MOF.

(B–D) (B) Cell viability of L02 cells incubated with different concentrations of Cu/EA-MOF. ($n = 3$) (C) Cell viability of SAM-pre-treated MC38 cells incubated with different concentrations of Cu/EA-MOF. ($n = 3$) (D) Cell viability of MC38 after different treatments. ($n = 3$) G1: control, G2: Cu/EA-MOF (200 μg mL^{-1}) + $ZnCl_2$, G3: EA-equivalent concentrations of EA, G4: Cu/EA-MOF (200 μg mL^{-1}), G5: Cu/EA-MOF (200 μg mL^{-1}) + SAM.

(E) Flow cytometric analysis of apoptosis in MC38 cells after different treatments.

(F) Colony formation assay of MC38 cells with different treatments. Data are shown as means ± SD.

coordination between the amino group of BBT and the copper ion (Figure S14).

MC38 cells exhibited significant NIR-II FL signals in both Cu/EA/BBT-MOF + SAM and Cu/EA/BBT-MOF + SAM + Cys groups, suggesting that overproduction of H_2S can trigger obvious FL recovery. By contrast, MC38 cells showed weak FL signal intensity in Cu/EA/BBT-MOF + $ZnCl_2$ group. A similar outcome was observed in the confocal FL imaging (Figure S15). The NIR-II FL signal intensity of cells with different treatments displayed a negative correlation with cell viability (Figure 5E). These results clearly implied that Cu/EA/BBT-MOF exhibited the capability of H_2S-activated NIR-II FL imaging, which can be used to monitor the disaggregation of Cu/EA-MOF. As a result of the good relationship between the NIR-II

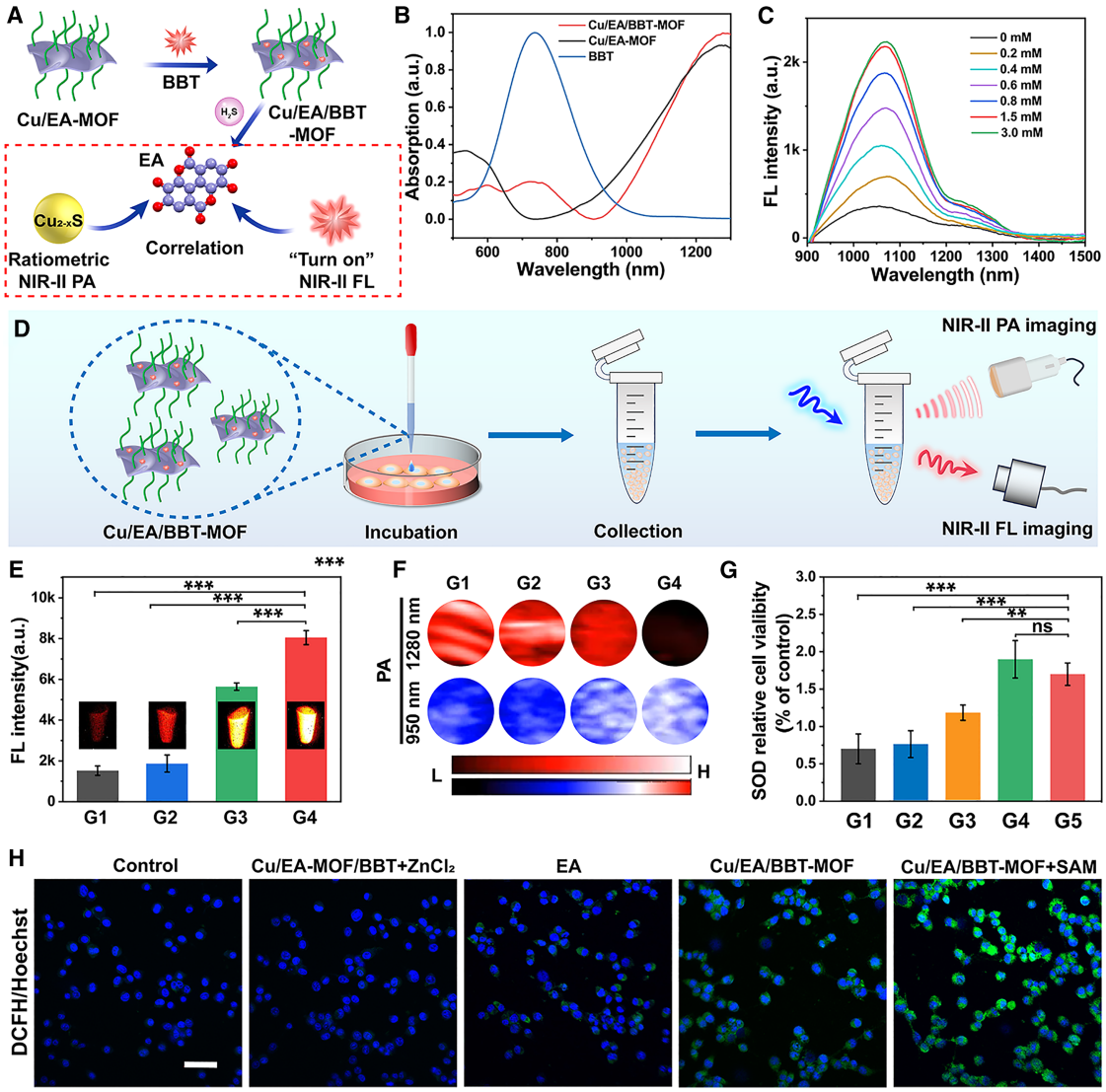

Figure 5. The synergistic therapy mechanism

(A) The correlation between NIR-II FL and ratiometric PA imaging and the formation of $Cu_{2-x}S$ and release of EA.

(B) Absorption spectra of Cu/EA-MOF, BBT, and Cu/EA/BBT-MOF.

(C) FL intensity of Cu/EA/BBT-MOF following addition of various concentrations of NaHS from 0 to 3.0 mM

(D) Schematic illustration of NIR-II FL and PA imaging of MC38 cells with different treatments.

(E) NIR-II FL imaging of MC38 cells and corresponding signal intensity at 1050 nm excited by 808 nm laser after different treatments. NIR-II FL images were collected in Eppendorf tubes (n = 3).

(F) NIR-II PA imaging of MC38 cells at 950 nm and 1280 nm with different treatments. G1: Cu/EA/BBT-MOF + $ZnCl_2$, G2: Cu/EA/BBT-MOF, G3: Cu/EA/BBT-MOF + SAM, G4: Cu/EA/BBT-MOF + SAM + L-Cys. L-Cysteine (L-Cys), a precursor for H_2S biosynthesis, was used to additionally enhance the endogenous H_2S levels in MC38 cells. NIR-II FL images were collected in Eppendorf tubes.

(G and H) (G) SOD activity in MC38 cells with different treatments. G1: PBS, G2: Cu/EA/BBT-MOF + $ZnCl_2$, G3: Cu/EA/BBT-MOF, G4: EA, G5: Cu/EA/BBT-MOF + SAM. (n = 3) (H) Confocal FL microscope images of DCFH-DA-stained MC38 cells (green fluorescence) after different treatments; scale bar: 50 μm. Data are shown as means ± SD.

(**p < 0.01, ***p < 0.001).

PA ratio and NaHS concentration in solution, the correlation between ratiometric NIR-II PA imaging and therapeutic effect was further uncovered *in vitro*. Cells showed the increased PA signal at 950 nm and decreased PA signal at 1280 nm with increasing H_2S levels tuned by different reagents, resulting in a significant change of ratiometric NIR-II PA ratio (Figures 5F and S16). Notably, the cell viability showed a strong negative correlation with the NIR-II PA intensity ratio, illustrating that Cu/EA/BBT-MOF could precisely predict the therapeutic outcome via the ratiometric NIR-II PA imaging (Figure S17). As shown in Figure 5G,

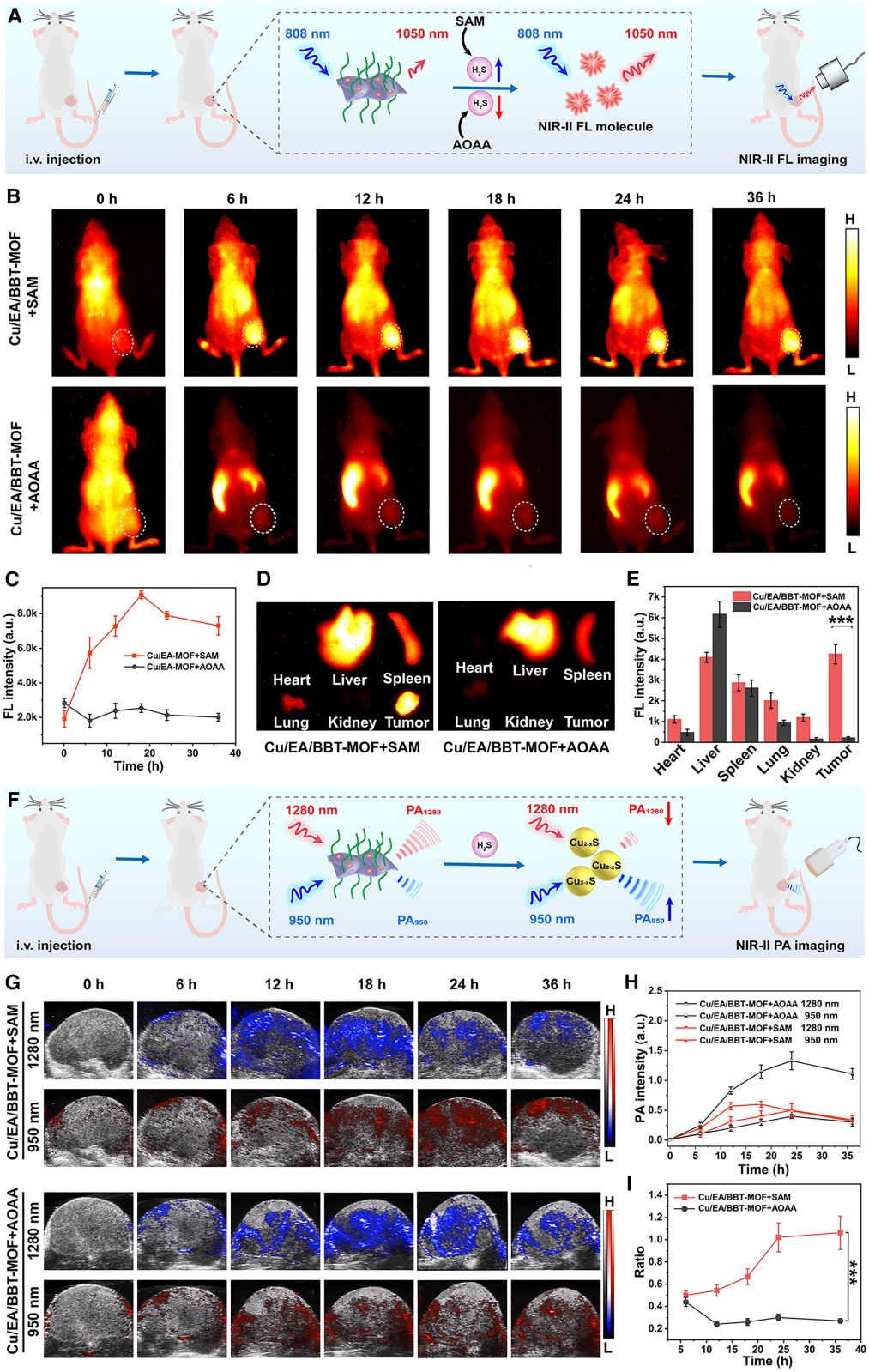

(legend on next page)

significantly higher SOD activity in MC38 cells was accidentally discovered in the presence of EA than in the absence of EA, indicating that EA can boost the SOD activity in MC38 cells. This result suggested that EA can induce an enhancement of H_2O_2 levels to promote the CDT effect of $Cu_{2-x}S$. The generation of intracellular ROS in MC38 cells was assessed using the intracellular ROS probe 2,7-dichlorofluorescin diacetate (DCFH-DA). Compared to the control and Cu/EA/BBT-MOF groups, the ROS level in the Cu/EA/BBT-MOF + SAM group was clearly higher, whereas a weaker FL intensity signal was observed in the Cu/EA/BBT-MOF + $ZnCl_2$ group (Figures 5H and S18). This discovery revealed the emergence of oxidative stress in cells, resulting from the H_2S-triggered Fenton-like reaction. Interestingly, MC38 cells treated with EA presented with only a slight increase in green FL intensity, testifying the enhancement of H_2O_2 levels. After C11-BODIPY staining for lipid peroxidation, Cu/EA/BBT-MOF treatment enhanced lipid peroxidation compared to the control and Cu/EA/BBT-MOF + $ZnCl_2$ group (Figure S19). In contrast, the cells treated with Cu/EA/BBT-MOF and SAM exhibited a more higher FL intensity signal, suggesting that the H_2S activated synergistic therapy. Comet assay was implemented to study the DNA damage in MC38 cells. A long comet tail was observed in the EA-treated cells, demonstrating that EA can cause DNA damage (Figure S20).

H_2S-responsive NIR-II FL/PA imaging *in vivo*

The excellent NIR-II FL and ratiometric NIR-II PA imaging capacity of Cu/EA/BBT-MOF induced by NaHS *in vitro* encouraged us to explore its efficacy in NIR-II PA/FL imaging of colon cancer. Hence, the mice bearing subcutaneous MC38 tumor xenografts were employed to further evaluate the H_2S-responsive imaging capability of Cu/EA/BBT-MOF. Mice were randomly split into three groups: (1) Cu/EA/BBT-MOF, pre-treated with PBS; (2) Cu/EA/BBT-MOF + AOAA, pre-treated with AOAA; and (3) Cu/EA/BBT-MOF + SAM, pre-treated with SAM. Pre-treatments were carried out for 24 h, followed by intravenous tail vein injection of Cu/EA/BBT-MOF. NIR-II FL images of mice at 1050 nm were captured at different time points (Figure 6A).

In the Cu/EA/BBT-MOF group, NIR-II FL signal was observed at the tumor site 6 h after intravenous injection of Cu/EA/BBT-MOF and reached a maximum 18 h after injection, resulting from the combination of the enhancement of H_2S-responsive FL signal and the enhanced permeability and retention (EPR) effect (Figure S21). In the Cu/EA-MOF + SAM group, the NIR-II FL signal intensity at 1050 nm was markedly increased in tumor tissues, which was attributed to the "turn on" behavior of Cu/EA/BBT-MOF in response to SAM-induced increases in H_2S concentration (Figure 6B). Cu/EA/BBT-MOF was degraded to $Cu_{2-x}S$ and BBT in response to H_2S after reaching the tumor. With the degradation of Cu/EA/BBT-MOF, tumor cells continuously produced BBT. The continuous uptake and degradation of Cu/EA/BBT-MOF by tumors lead to the ability of sustained fluorescence imaging. Moreover, the structure of BBT contained amino groups, which can easily bind to macromolecules within the tumor and linger in the tumor.[48,49] Owing to AOAA-induced inhibition of H_2S generation, negligible NIR-II FL signal at 1050 nm was detected at the tumor site in the Cu/EA/BBT-MOF + AOAA group over the same time period compared to that in the Cu/EA/BBT-MOF and Cu/EA/BBT-MOF + SAM groups (Figure 6C). The NIR-II FL images of *ex vivo* tumors and organs confirmed that the FL signal of Cu/EA/BBT-MOF can be successfully turned on by endogenous H_2S (Figures 6D and 6E). By comparing the three groups, we found that the imaging ability of Cu/EA/BBT-MOF in tumors was correlated with the expression level of H_2S. It suggested that Cu/EA/BBT-MOF imaging could semi-quantitatively show the expression level of H_2S in tumors. Cu/EA/BBT-MOF has great potential for semi-quantitative analysis of H_2S. These results suggested that the H_2S-triggered NIR-II FL imaging could be used for monitoring the decomposition of Cu/EA/BBT-MOF.

However, single intensity-dependent signal of FL imaging is difficult to achieve precise monitoring. Therefore, we proceeded to evaluate ratiometric NIR-II PA imaging ability of Cu/EA/BBT-MOF *in vivo* (Figure 6F). The PA intensity increment (ΔPA) was calculated by subtracting the intrinsic PA intensity of the tumor tissue before Cu/EA/BBT-MOF injection from the PA signal after Cu/EA/BBT-MOF injection to minimize the tumor tissue interference. After intravenous administration, both accumulation of Cu/EA/BBT-MOF in the tumor and the conversion from Cu/EA/BBT-MOF to $Cu_{2-x}S$ could be visualized using the gradual changes of ΔPA_{1280} and ΔPA_{950} signal intensity (Figure S22). In the pre-treated inhibitor group, the ΔPA_{1280} signal increased significantly due to the EPR effect and the low level of H_2S (Figures 6G and 6H). A high ΔPA_{1280} signal and a low ΔPA_{950} signal were observed at the tumor site, showing no significant change in the low ratio value (Figure 6I). However, the H_2S levels in tumors can be upregulated after SAM pretreatment, leading to a low ΔPA_{1280} signal and a high ΔPA_{950} signal. Meanwhile, the ratio between ΔPA_{950} and ΔPA_{1280} drastically increased. Taken together, these findings demonstrate that Cu/EA/BBT-MOF can react with overexpressed H_2S in the colorectal tumors to form $Cu_{2-x}S$, endowing the ratiometric NIR-II PA imaging to monitor the EA release and $Cu_{2-x}S$ generation.

In vivo antitumor efficacy

Encouraged by the H_2S-triggered therapeutic effect *in vitro* and ratiometric NIR-II PA imaging *in vivo*, we further studied the

Figure 6. H_2S-responsive NIR-II FL/PA imaging *in vivo*

(A) Schematic illustration of H_2S-responsive NIR-II FL imaging in MC38 tumors during therapy.
(B) NIR-II FL imaging of mice after different treatments.
(C) Relative NIR-II FL signal intensity at 1,050 nm of (B).
(D and E) *Ex vivo* NIR-II FL imaging and relative NIR-II FL signal intensity of major organs 24 h after intravenous injection of Cu/EA/BBT-MOF.
(F) Schematic illustration of H_2S-triggered ratiometric NIR-II PA imaging in MC38 tumors during therapy.
(G) Representative NIR-II PA cross-sectional imaging of tumor sites in tumor-bearing mice after different treatments.
(H and I) Relative NIR-II PA signal intensity and ratio of (G). Data are shown as means ± SD.
(***$p < 0.001$, $n = 3$).

therapeutic effect of Cu/EA/BBT-MOF activated by endogenous H_2S *in vivo* using the MC38-tumor-bearing mice model. Before administration to mice, the hemolysis tests were conducted to explore the blood safety of Cu/EA/BBT-MOF. The hemolysis rates below 5% were found over a wide range of concentration (0–1.5 mg mL^{-1}), proving the good blood compatibility of Cu/EA/BBT-MOF (Figure S23).

As a standard method, all mice were randomly divided into five groups, including PBS, EA, Cu/EA/BBT-MOF, Cu/EA/BBT-MOF + SAM, and Cu/EA/BBT-MOF + AOAA. The mice were respectively pretreated with SAM and AOAA in Cu/EA/BBT-MOF + SAM group and Cu/EA/BBT-MOF + AOAA group, aiming to upregulate and inhibit the level of endogenous H_2S in tumor. The treatment was repeated four times at a period of every 3 days, and tumor volume was recorded for 16 days (Figure 7A). The tumor of mice in PBS group grew rapidly, growing in volume by 16-fold after 16 days (Figures 7B and 7C). Compared to the PBS control, EA or Cu/EA/BBT-MOF slightly inhibited tumor growth. Previous studies have demonstrated that EA presented anti-tumor efficacy through multifaceted mechanisms, including inducing tumor cell apoptosis, suppressing tumor cell proliferation, and other pathways of inhibiting the growth of cancer cells.[38,50] The tumor growth rate in Cu/EA/BBT-MOF + SAM group was significantly inhibited, which attributed to the enhancing synergistic therapeutic effect of EA and $Cu_{2-x}S$. In contrast, the tumor growth rate of mice pretreated with AOAA was similar to that of the control, suggesting endogenous H_2S-responsive therapeutic effect. On the 16th day, the tumor inhibition rates of the EA, Cu/EA/BBT-MOF, Cu/EA/BBT-MOF + SAM, and Cu/EA/BBT-MOF + AOAA treatment groups were approximately 36.1%, 25.1%, 83.7%, and 8.5%, respectively. These results revealed the excellent antitumor efficiency of Cu/EA/BBT-MOF in tumors containing endogenous H_2S. It also illustrated that the anti-tumor ability of Cu/EA/BBT-MOF were correlated with the expression level of H_2S in tumor.

The relationship between ratiometric NIR-II PA imaging signal and the late-time therapeutic outcomes in MC38 mouse models were further investigated. The corresponding relative tumor volume changes were strongly negatively correlated with NIR-II PA ratios, indicating the early prediction ability of *in vitro* and *in vivo* therapy efficacy of Cu/EA/BBT-MOF (Figure 7D). Cu/EA/BBT-MOF can remarkably prolong the survival of mice pre-treated with SAM (Figure 7E). Negligible loss in body weight was observed in mice treated with Cu/EA/BBT-MOF during the therapy period of 16 days (Figure 7F). Furthermore, the representative hematoxylin and eosin (H&E) staining of the tumors displayed obvious necrosis of tumor cells in the Cu/EA/BBT-MOF + SAM group *in vivo*, which further verified that H_2S-triggered the therapeutic effect of Cu/EA/BBT-MOF (Figure 7G). To further elucidate the underlying mechanism of the excellent antitumor performance of Cu/EA/BBT-MOF, Ki67, and TUNEL FL staining were carried out. These results verified that Cu/EA/BBT-MOF could induce significant apoptosis and seriously inhibited cell proliferation in tumors in Cu/EA/BBT-MOF + SAM group (Figure 7H).

The *in vivo* biosafety of nanoparticles was then evaluated. Firstly, H&E staining of the major organs (e.g., heart, liver, spleen, lung, and kidney) revealed that negligible pathophysiological damage was observed in either the Cu/EA/BBT-MOF or PBS group (Figure S24). Additionally, serum biochemistry analyses indicated similar biochemical parameters between PBS and Cu/EA/BBT-MOF groups (Figure S25). These results disclosed the excellent biosafety of Cu/EA/BBT-MOF.

DISCUSSION

In summary, we constructed a theranostic Cu/EA/BBT-MOF containing Cu^{2+} ions and phenolic drug for colon cancer imaging and treatment. Benefiting from the intrinsic NIR-II PA imaging ability of Cu/EA/BBT-MOF, the $Cu_{2-x}S$ generation and EA release can be accurately monitored, which can be further applied to predict the therapeutic outcome. The prepared Cu/EA/BBT-MOF could be activated by endogenous H_2S and induce apoptosis by synergistic chemo/chemodynamic therapy. The $Cu_{2-x}S$ was formed from the reaction between Cu/EA/BBT-MOF and H_2S, resulting in a dramatic variation of NIR-II PA signal intensity ratios. Based on the distinct switch in NIR-II PA ratios, Cu/EA/BBT-MOF permitted real-time and non-invasive imaging of activated therapy process, detecting the generation of agents responsible for the therapeutic effects during endogenous H_2S-triggered synergistic therapy. Experiments showed that Cu/EA/BBT-MOF can obviously inhibit tumor growth and prolong overall survival. Observed variations in NIR-II PA ratios correlated well with the therapeutic outcomes. This study has established a simple strategy for both diagnosis and treatment of colon cancer guided by ratiometric NIR-II PA imaging, which was assisted to achieve precise therapy.

Limitations of the study

The performance of nanomaterials has not been validated in the *in situ* colon cancer models. The application of the nanomaterials in the *in situ* colon model can better illustrate the endogenous H_2S-activated combination therapy of chemodynamic therapy and chemotherapy. Furthermore, the application of nanomaterials in the *in situ* colon cancer models can more effectively show the advantages of NIR-II FL and PA imaging.

RESOURCE AVAILABILITY

Lead contact

Further information and requests for resources should be directed to and will be fulfilled by the lead contact, Shi Gao (gaoshi@jlu.edu.cn).

Materials availability

No new materials were created during this study.

Data and code availability

- Data reported in this paper will be shared by the lead contact upon request.
- This paper does not report original code.
- Any additional information required to reanalyze the data reported in this work paper is available from the lead contact upon request.

ACKNOWLEDGMENTS

This work was supported by the National Natural Science Foundation of China (no. 82272033, U22A20348, 82071960, and U1867210), the Hygiene Specific Subjects of Jilin Province (no. 2022SCZ27, 2023SCZ29, and

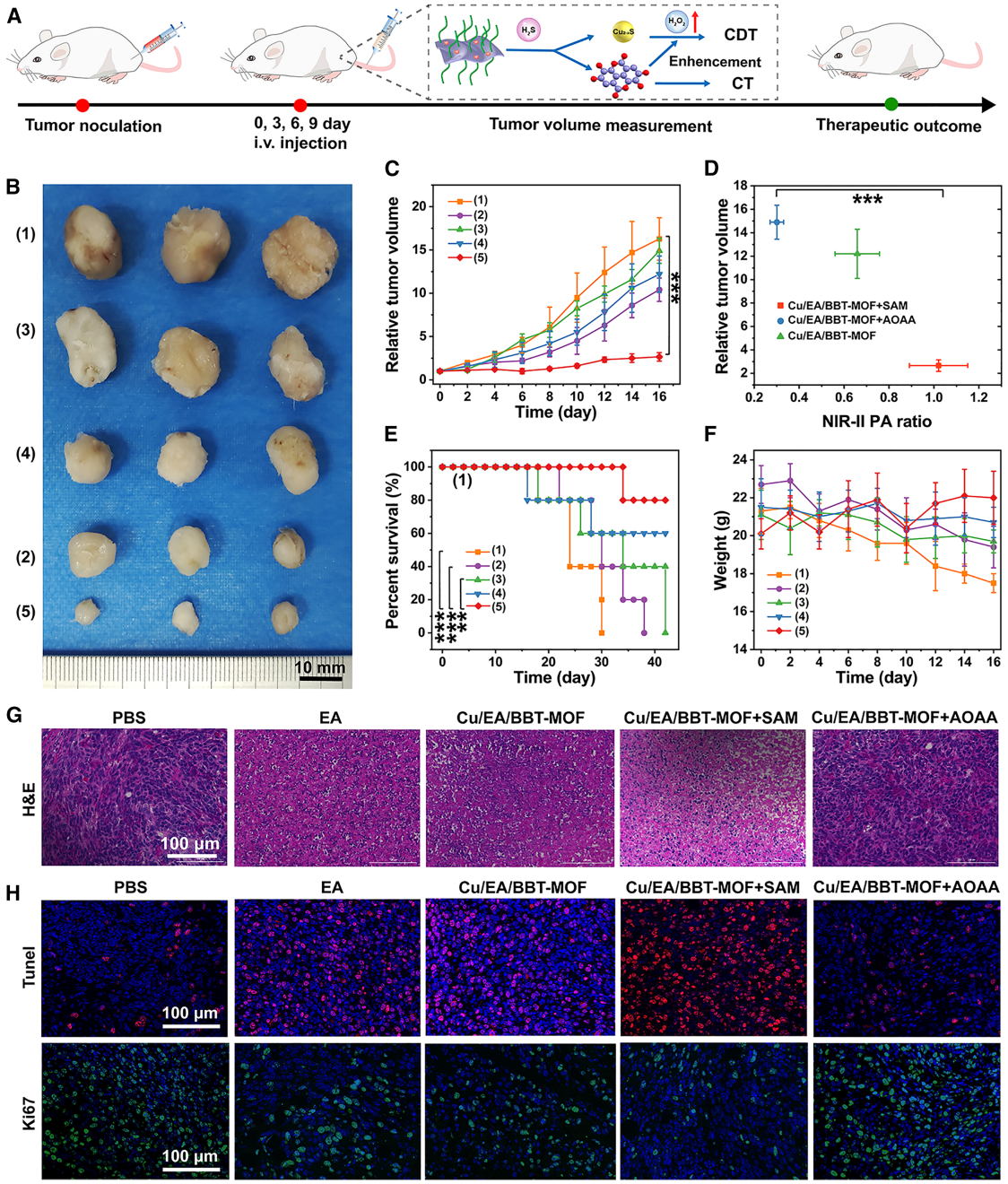

Figure 7. ***In vivo*** **antitumor efficacy**

(A) Schematic illustration of therapy in MC38 tumor-bearing mice.

(B) Photographs of tumors excised from mice with different treatments. Scale bars: 10 mm

(C) Relative tumor volumes of tumor-bearing mice with different treatments (Means ± SD; $n = 3$).

(D) Correlation between the relative tumor volume at day 16 and the corresponding ratiometric NIR-II PA signal intensities after synergistic therapy.

(E) Relative survival curves of mice treated with different treatments ($n = 5$).

(F) The body weights of mice during different treatments ($n = 3$).

(G) H&E staining of tumor slices from different treatment groups. Scale bars: 100 μm

(H) TUNEL staining of tumors. Scale bars: 100 μm. Data are shown as means ± SD.

(**$p < 0.01$, ***$p < 0.001$; (1) PBS, (2) EA, (3) Cu/EA/BBT-MOF+AOAA, (4) Cu/EA/BBT-MOF, (5) Cu/EA/BBT-MOF+SAM.).

2021SCZ18), and Jilin Scientific and Technological Development Program (no. 20210101445JC).

AUTHOR CONTRIBUTIONS

W.Z. was responsible for formal analysis, writing-original draft, methodology, investigation, and data curation; M.Z. was responsible for investigation; L.W. participated in formal analysis and investigation; J.W. participated in formal analysis and investigation; X.G. participated in investigation; J. Liu participated in project administration and funding acquisition; B.C. participated in project administration and funding acquisition; S.G. participated in writing-original draft, supervision, funding acquisition, and conceptualization; J. Lu participated in writing-original draft, supervision, funding acquisition, and conceptualization.

DECLARATION OF INTERESTS

The authors declare no competing interests.

STAR★METHODS

Detailed methods are provided in the online version of this paper and include the following:

- KEY RESOURCES TABLE
- EXPERIMENTAL MODEL AND STUDY PARTICIPANT DETAILS
  - Cell culture
  - Animal model
- METHOD DETAILS
  - Synthesis
  - *In vitro* H_2S-responsive behavior
  - *In vitro* drug release
  - Cell toxicity test
  - Evaluation of intercellular ROS
  - NIR-II FL and PA imaging of cells
  - *In vivo* NIR-II FL and PA imaging of mice
  - Therapeutic efficiency *in vivo*
- QUANTIFICATION AND STATISTICAL ANALYSIS

SUPPLEMENTAL INFORMATION

Supplemental information can be found online at https://doi.org/10.1016/j.isci.2025.112425.

Received: January 16, 2025
Revised: March 16, 2025
Accepted: April 9, 2025
Published: April 14, 2025

REFERENCES

1. Zhang, B., Hou, X.L., Xie, X.T., Tan, L.F., Guan, M., Zhao, D.H., Zhou, S., Cheng, K., Fan, J.X., and Liu, B. (2024). Nanoplatforms derived from iron dextran combined with ascorbic acid for enhanced photothermal-chemodynamic therapy of tumors. Chem. Eng. J. *496*, 154044. https://doi.org/10.1016/j.cej.2024.154044.
2. Zhou, Y., Li, Q., Wu, Y., Li, X., Zhou, Y., Wang, Z., Liang, H., Ding, F., Hong, S., Steinmetz, N.F., and Cai, H. (2023). Molecularly Stimuli-Responsive Self-Assembled Peptide Nanoparticles for Targeted Imaging and Therapy. ACS Nano *17*, 8004–8025. https://doi.org/10.1021/acsnano.3c01452.
3. Ding, C., Chen, C., Zeng, X., Chen, H., and Zhao, Y. (2022). Emerging Strategies in Stimuli-Responsive Prodrug Nanosystems for Cancer Therapy. ACS Nano *16*, 13513–13553. https://doi.org/10.1021/acsnano.2c05379.
4. Li, Z., Xu, K., Qin, L., Zhao, D., Yang, N., Wang, D., and Yang, Y. (2023). Hollow Nanomaterials in Advanced Drug Delivery Systems: From Single- to Multiple Shells. Adv. Mater. *35*, 2203890. https://doi.org/10.1002/adma.202203890.
5. Baek, J., Song, N., Yoo, B., Lee, D., and Kim, B.-S. (2024). Precisely Programmable Degradation and Drug Release Profiles in Triblock Copolyether Hydrogels with Cleavable Acetal Pendants. J. Am. Chem. Soc. *146*, 13836–13845. https://doi.org/10.1021/jacs.3c14838.
6. Liu, H., Zhao, J., Xue, Y., Zhang, J., Bai, H., Pan, S., Peng, B., Li, L., and Voelcker, N.H. (2023). X-Ray-Induced Drug Release for Cancer Therapy. Angew. Chem. Int. Ed. *62*, e202306100. https://doi.org/10.1002/anie.202306100.
7. Zelepukin, I.V., Griaznova, O.Y., Shevchenko, K.G., Ivanov, A.V., Baidyuk, E.V., Serejnikova, N.B., Volovetskiy, A.B., Deyev, S.M., and Zvyagin, A.V. (2022). Flash drug release from nanoparticles accumulated in the targeted blood vessels facilitates the tumour treatment. Nat. Commun. *13*, 6910. https://doi.org/10.1038/s41467-022-34718-3.
8. Zeng, L., Ding, S., Cao, Y., Li, C., Zhao, B., Ma, Z., Zhou, J., Hu, Y., Zhang, X., Yang, Y., et al. (2023). A MOF-Based Potent Ferroptosis Inducer for Enhanced Radiotherapy of Triple Negative Breast Cancer. ACS Nano *17*, 13195–13210. https://doi.org/10.1021/acsnano.3c00048.
9. Chen, Z., Sun, Y., Wang, J., Zhou, X., Kong, X., Meng, J., and Zhang, X. (2023). Dual-Responsive Triple-Synergistic Fe-MOF for Tumor Theranostics. ACS Nano *17*, 9003–9013. https://doi.org/10.1021/acsnano.2c10310.
10. Xu, Z., Zhen, W., McCleary, C., Luo, T., Jiang, X., Peng, C., Weichselbaum, R.R., and Lin, W. (2023). Nanoscale Metal–Organic Framework with an X-ray Triggerable Prodrug for Synergistic Radiotherapy and Chemotherapy. J. Am. Chem. Soc. *145*, 18698–18704. https://doi.org/10.1021/jacs.3c04602.
11. Yang, J., Dai, D., Zhang, X., Teng, L., Ma, L., and Yang, Y.W. (2023). Multifunctional Metal-organic Framework (MOF)-based Nanoplatforms for Cancer Therapy: from Single to Combination Therapy. Theranostics *13*, 295–323. https://doi.org/10.7150/thno.80687.
12. Ma, Y., Li, X., Li, A., Yang, P., Zhang, C., and Tang, B. (2017). H(2)S-Activable MOF Nanoparticle Photosensitizer for Effective Photodynamic Therapy against Cancer with Controllable Singlet-Oxygen Release. Angew. Chem. Int. Ed. *56*, 13752–13756. https://doi.org/10.1002/anie.201708005.
13. Zhao, F., Yu, H., Liang, L., Wang, C., Shi, D., Zhang, X., Ying, Y., Cai, W., Li, W., Li, J., et al. (2023). Redox Homeostasis Disruptors Based on Metal-Phenolic Network Nanoparticles for Chemo/Chemodynamic Synergistic Tumor Therapy through Activating Apoptosis and Cuproptosis. Adv. Healthc. Mater. *12*, 2301346. https://doi.org/10.1002/adhm.202301346.
14. Zhang, M., Wang, L., Jin, H., Zhao, N., Liu, Y., Lan, S., Liu, S., and Zhang, H. (2023). Employing Single Valency Polyphenol to Prepare Metal-phenolic Network Antitumor Reagents through FeOOH Assistance. J. Control. Release *358*, 612–625. https://doi.org/10.1016/j.jconrel.2023.05.020.
15. Liu, Z., Liu, S., Liu, B., Bian, Y., Yuan, M., Yang, C., Meng, Q., Chen, C., Ma, P., and Lin, J. (2023). Fe(III)-Naphthazarin Metal-Phenolic Networks for Glutathione-Depleting Enhanced Ferroptosis-Apoptosis Combined Cancer Therapy. Small *19*, e2207825. https://doi.org/10.1002/smll.202207825.
16. Liu, J., Yuan, Y., Cheng, Y., Fu, D., Chen, Z., Wang, Y., Zhang, L., Yao, C., Shi, L., Li, M., et al. (2022). Copper-Based Metal–Organic Framework Overcomes Cancer Chemoresistance through Systemically Disrupting Dynamically Balanced Cellular Redox Homeostasis. J. Am. Chem. Soc. *144*, 4799–4809. https://doi.org/10.1021/jacs.1c11856.
17. Dai, Q., Geng, H., Yu, Q., Hao, J., and Cui, J. (2019). Polyphenol-Based Particles for Theranostics. Theranostics *9*, 3170–3190. https://doi.org/10.7150/thno.31847.
18. Yan, J., Li, W., Tian, H., Li, B., Yu, X., Wang, G., Sang, W., and Dai, Y. (2023). Metal-Phenolic Nanomedicines Regulate T-Cell Antitumor Function for Sono-Metabolic Cancer Therapy. ACS Nano *17*, 14667–14677. https://doi.org/10.1021/acsnano.3c02428.

19. Wang, G., Li, B., Tian, H., Xie, L., Yan, J., Sang, W., Li, J., Zhang, Z., Li, W., and Dai, Y. (2023). A Metal–Phenolic Nanocoordinator Launches Radiotherapeutic Cancer Pyroptosis Through an Epigenetic Mechanism. Adv. Funct. Mater. *33*, 2213425. https://doi.org/10.1002/adfm.202213425.

20. Li, X., Duan, Z., Chen, X., Pan, D., Luo, Q., Gu, L., Xu, G., Li, Y., Zhang, H., Gong, Q., et al. (2023). Impairing Tumor Metabolic Plasticity via a Stable Metal-Phenolic-Based Polymeric Nanomedicine to Suppress Colorectal Cancer. Adv. Mater. *35*, e2300548. https://doi.org/10.1002/adma.202300548.

21. Li, J., Zhou, Y., Liu, J., Yang, X., Zhang, K., Lei, L., Hu, H., Zhang, H., Ouyang, L., and Gao, H. (2022). Metal-phenolic Networks with Ferroptosis to Deliver NIR-responsive CO for Synergistic Therapy. J. Control. Release *352*, 313–327. https://doi.org/10.1016/j.jconrel.2022.10.025.

22. Xie, L., Li, J., Wang, G., Sang, W., Xu, M., Li, W., Yan, J., Li, B., Zhang, Z., Zhao, Q., et al. (2022). Phototheranostic Metal-Phenolic Networks with Antiexosomal PD-L1 Enhanced Ferroptosis for Synergistic Immunotherapy. J. Am. Chem. Soc. *144*, 787–797. https://doi.org/10.1021/jacs.1c09753.

23. Zhang, L., Wang, Z., Zhang, R., Yang, H., Wang, W.-J., Zhao, Y., He, W., Qiu, Z., Wang, D., Xiong, Y., et al. (2023). Multi-Stimuli-Responsive and Cell Membrane Camouflaged Aggregation-Induced Emission Nanogels for Precise Chemo-photothermal Synergistic Therapy of Tumors. ACS Nano *17*, 25205–25221. https://doi.org/10.1021/acsnano.3c08409.

24. Zhao, X., He, S., Li, B., Liu, B., Shi, Y., Cong, W., Gao, F., Li, J., Wang, F., Liu, K., et al. (2023). DUCNP@Mn-MOF/FOE as a Highly Selective and Bioavailable Drug Delivery System for Synergistic Combination Cancer Therapy. Nano Lett. *23*, 863–871. https://doi.org/10.1021/acs.nanolett.2c04042.

25. Lacerda, S., Delalande, A., Eliseeva, S.V., Pallier, A., Bonnet, C.S., Szeremeta, F., Même, S., Pichon, C., Petoud, S., and Tóth, É. (2021). Doxorubicin-Sensitized Luminescence of NIR-Emitting Ytterbium Liposomes: Towards Direct Monitoring of Drug Release. Angew. Chem. Int. Ed. *60*, 23574–23577. https://doi.org/10.1002/anie.202109408.

26. Liu, Y., Yang, G., Jin, S., Zhang, R., Chen, P., Zhao, C.X., Tengjisi, Wang, L., Wang, L., Chen, D., and Weitz, D.A. (2020). J-Aggregate-Based FRET Monitoring of Drug Release from Polymer Nanoparticles with High Drug Loading. Angew. Chem. Int. Ed. *59*, 20065–20074. https://doi.org/10.1002/anie.202008018.

27. Zhang, Y., Yan, C., Zheng, Q., Jia, Q., Wang, Z., Shi, P., and Guo, Z. (2021). Harnessing Hypoxia-Dependent Cyanine Photocages for In Vivo Precision Drug Release. Angew. Chem. Int. Ed. *60*, 9553–9561. https://doi.org/10.1002/anie.202017349.

28. Li, J., Wang, J., Xu, L., Chi, H., Liang, X., Yoon, J., and Lin, W. (2024). A Class of Activatable NIR-II Photoacoustic Dyes for High-Contrast Bioimaging. Angew. Chem. Int. Ed. *63*, e202312632. https://doi.org/10.1002/anie.202312632.

29. Zeng, S., Chen, J., Gao, R., Chen, R., Xue, Q., Ren, Y., Liu, L., Tang, C., Hu, H., Zeng, N., et al. (2024). NIR-II Photoacoustic Imaging-Guided Oxygen Delivery and Controlled Release Improves Photodynamic Therapy for Hepatocellular Carcinoma. Adv. Mater. *36*, 2308780. https://doi.org/10.1002/adma.202308780.

30. Wang, S., Zhang, X., Zhang, Y., Zhu, K., Liu, X., Zhang, J., Wang, G., Liu, D., Zhao, K., Wang, X., et al. (2023). Activatable Nanoprobes for Dual-Modal NIR-II Photoacoustic and Fluorescence Imaging of Hydrogen Sulfide in Colon Cancer. Adv. Opt. Mater. *12*, 2302796. https://doi.org/10.1002/adom.202302796.

31. Su, L., Tang, H., Liao, N., Chen, Z., Li, H., Ge, X., Wu, Y., Li, Q., Zhang, X., Chen, J., et al. (2023). Spatiotemporally confined assembly of radiosensitizers for synergistic radio-chemodynamic therapy on deep tumor of rabbit. Nano Today *50*, 101835. https://doi.org/10.1016/j.nantod.2023.101835.

32. Zheng, X., Kang, W., Jin, Y., Zhang, X., Wang, W., Li, D., Wu, S., Chen, L., Meng, S., Dai, R., et al. (2024). In-situ GSH-responsive gas nanogenerator for active NIR-II FL/PA imaging and synergistic restoration the macrophage niche in rheumatoid arthritis. Chem. Eng. J. *485*, 150128. https://doi.org/10.1016/j.cej.2024.150128.

33. Chen, T., Su, L., Ge, X., Zhang, W., Li, Q., Zhang, X., Ye, J., Lin, L., Song, J., and Yang, H. (2020). Dual activated NIR-II fluorescence and photoacoustic imaging-guided cancer chemo-radiotherapy using hybrid plasmonic-fluorescent assemblies. Nano Res. *13*, 3268–3277. https://doi.org/10.1007/s12274-020-3000-9.

34. Jiang, Z., Zhang, C., Wang, X., Ling, Z., Chen, Y., Guo, Z., and Liu, Z. (2024). A Small-Molecule Ratiometric Photoacoustic Probe for the High-Spatiotemporal-Resolution Imaging of Copper(II) Dynamics in the Mouse Brain. Angew. Chem. Int. Ed. *63*, e202318340. https://doi.org/10.1002/anie.202318340.

35. Fu, Q., Yang, X., Wang, M., Zhu, K., Wang, Y., and Song, J. (2024). Activatable Probes for Ratiometric Imaging of Endogenous Biomarkers In Vivo. ACS Nano *18*, 3916–3968. https://doi.org/10.1021/acsnano.3c10659.

36. Zhu, K., Zhang, X., Wu, Y., and Song, J. (2023). Ratiometric Optical and Photoacoustic Imaging in the Second Near-Infrared Window. Acc. Chem. Res. *56*, 3223–3234. https://doi.org/10.1021/acs.accounts.3c00495.

37. Lu, G., Wang, X., Cheng, M., Wang, S., and Ma, K. (2023). The Multifaceted Mechanisms of Ellagic Acid in the Treatment of Tumors: State-of-the-art. Biomed. Pharmacother. *165*, 115132. https://doi.org/10.1016/j.biopha.2023.115132.

38. Kim, S., Gaber, M.W., Zawaski, J.A., Zhang, F., Richardson, M., Zhang, X. A., and Yang, Y. (2009). The inhibition of glioma growth in vitro and in vivo by a chitosan/ellagic acid composite biomaterial. Biomaterials *30*, 4743–4751. https://doi.org/10.1016/j.biomaterials.2009.05.010.

39. Lu, S., Tian, H., Li, B., Li, L., Jiang, H., Gao, Y., Zheng, L., Huang, C., Zhou, Y., Du, Z., and Xu, J. (2024). An Ellagic Acid Coordinated Copper-Based Nanoplatform for Efficiently Overcoming Cancer Chemoresistance by Cuproptosis and Synergistic Inhibition of Cancer Cell Stemness. Small *20*, 2309215. https://doi.org/10.1002/smll.202309215.

40. An, L., Wang, X., Rui, X., Lin, J., Yang, H., Tian, Q., Tao, C., and Yang, S. (2018). The In Situ Sulfidation of Cu_2O by Endogenous H_2S for Colon Cancer Theranostics. Angew. Chem. Int. Ed. *57*, 15782–15786. https://doi.org/10.1002/anie.201810082.

41. Wu, L., Ishigaki, Y., Hu, Y., Sugimoto, K., Zeng, W., Harimoto, T., Sun, Y., He, J., Suzuki, T., Jiang, X., et al. (2020). H_2S-activatable near-infrared afterglow luminescent probes for sensitive molecular imaging in vivo. Nat. Commun. *11*, 446–514. https://doi.org/10.1038/s41467-020-14307-y.

42. Shi, B., Ren, N., Gu, L., Xu, G., Wang, R., Zhu, T., Zhu, Y., Fan, C., Zhao, C., and Tian, H. (2019). Theranostic Nanoplatform with Hydrogen Sulfide Activatable NIR Responsiveness for Imaging-Guided On-Demand Drug Release. Angew. Chem. Int. Ed. Engl. *58*, 16826–16830. https://doi.org/10.1002/anie.201909883.

43. Kolluru, G.K., Shen, X., Bir, S.C., and Kevil, C.G. (2013). Hydrogen sulfide chemical biology: Pathophysiological roles and detection. Nitric Oxide *35*, 5–20. https://doi.org/10.1016/j.niox.2013.07.002.

44. Li, S., Ma, Q., Wang, C., Yang, K., Hong, Z., Chen, Q., Song, J., Song, X., and Yang, H. (2022). Near-Infrared II Gold Nanocluster Assemblies with Improved Luminescence and Biofate for In Vivo Ratiometric Imaging of H2S. Anal. Chem. *94*, 2641–2647. https://doi.org/10.1021/acs.analchem.1c05154.

45. Hu, Q., Zhu, C., Hankins, R.A., Murmello, A.R., Marrs, G.S., and Lukesh, J. C. (2023). An ROS-Responsive Donor That Self-Reports Its H2S Delivery by Forming a Benzoxazole-Based Fluorophore. J. Am. Chem. Soc. *145*, 25486–25494. https://doi.org/10.1021/jacs.3c10446.

46. Wu, R., Chen, Z., Huo, H., Chen, L., Su, L., Zhang, X., Wu, Y., Yao, Z., Xiao, S., Du, W., and Song, J. (2022). Ratiometric Detection of H2S in Liver Injury by Activated Two-Wavelength Photoacoustic Imaging. Anal. Chem. *94*, 10797–10804. https://doi.org/10.1021/acs.analchem.2c01571.

47. Ge, X., Su, L., Chen, Z., Zhu, K., Zhang, X., Wu, Y., and Song, J. (2023). A Radio-Pharmaceutical Fluorescent Probe for Synergistic Cancer Radiotherapy and Ratiometric Imaging of Tumor Reactive Oxygen Species. Angew. Chem. Int. Ed. Engl. *62*, 202305744. https://doi.org/10.1002/anie.202305744.

48. Grkovski, M., Schöder, H., Lee, N.Y., Carlin, S.D., Beattie, B.J., Riaz, N., Leeman, J.E., O'Donoghue, J.A., and Humm, J.L. (2017). Multiparametric Imaging of Tumor Hypoxia and Perfusion with ^{18}F-Fluoromisonidazole Dynamic PET in Head and Neck Cancer. J. Nucl. Med. *58*, 1072–1080. https://doi.org/10.2967/jnumed.116.188649.

49. Ruiz de Garibay, G., García de Jalón, E., Stigen, E., Lund, K.B., Popa, M., Davidson, B., Safont, M.M., Rygh, C.B., Espedal, H., Barrett, T.M., et al. (2021). Repurposing ^{18}F-FMISO as a PET tracer for translational imaging of nitroreductase-based gene directed enzyme prodrug therapy. Theranostics *11*, 6044–6057. https://doi.org/10.7150/thno.55092.

50. Lu, G., Wang, X., Cheng, M., Wang, S., and Ma, K. (2023). The multifaceted mechanisms of ellagic acid in the treatment of tumors: State-of-the-art. Biomed. Pharmacother. *165*, 115132. https://doi.org/10.1016/j.biopha.2023.115132.

51. Schindelin, J., Arganda-Carreras, I., Frise, E., Kaynig, V., Longair, M., Pietzsch, T., Preibisch, S., Rueden, C., Saalfeld, S., Schmid, B., et al. (2012). Fiji: an open-source platform for biological-image analysis. Nat. Methods *9*, 676–682. https://doi.org/10.1038/nmeth.2019.

STAR★METHODS

KEY RESOURCES TABLE

REAGENT or RESOURCE	SOURCE	IDENTIFIER
Chemicals, peptides, and recombinant proteins		
$Cu(NO_3)_2{\cdot}3H_2O$	Sigma Aldrich	Cat: 61194, CAS: 10031-43-3
Ellagic acid (EA)	Sigma Aldrich	Cat: 14668, CAS: 476-66-4
Polyvinyl pyrrolidone (PVP)	Sigma Aldrich	Cat: PVP40, CAS: 9003-39-8
Ethanol	Sigma Aldrich	Cat: 1009831011, CAS: 64-17-5
NaSH	Aladdin	Cat: S106641, CAS:207683-19-0
Tris-HCl buffer	Aladdin	Cat: T301509
Phosphate-buffered saline (PBS)	Sigma Aldrich	Cat: P4474
H_2O_2	Aladdin	Cat: H112520, CAS: 7722-84-1
$ZnCl_2$	Aladdin	Cat: Z112534, CAS: 7646-85-7
S-adenosyl-L-methionine (SAM)	Aladdin	Cat: S192607, CAS: 29908-03-0
Aminooxyacetic acid (AOAA)	Aladdin	Cat: A607614, CAS: 645-88-5
L-Cysteine (L-Cys)	Aladdin	Cat: C108238, CAS: 52-90-4
NaCl	Aladdin	Cat: C111547, CAS: 7647-14-5
Na_2SO_4	Aladdin	Cat: S433908, CAS: 7757-82-6
Na_2CO_3	Aladdin	Cat: S432757, CAS: 497-19-8
NaH_2PO_4	Aladdin	Cat: S108343, CAS: 7558-80-7
Glutathione (GSH)	Sigma Aldrich	Cat: Y0000517, CAS: 70-18-8
Cyanine dye Cy5	Aladdin	Cat: C288764, CAS: 146368-14-1
Critical commercial assays		
Reactive oxygen species (ROS) assay kit	Beyotime Biotechnology (Shanghai, China)	Cat: S0061S
Lipid peroxide (LPO) fluorometric assay kit	Elabscience Biotechnology Co., Ltd	Cat: E-BC-F003
Aspartate aminotransferase assay kit (AST)	NanJing Jiancheng Bioengineering Institute	Cat: C010-3-1
alanine aminotransferase assay kit (ALT)	NanJing Jiancheng Bioengineering Institute	Cat: C009-3-1
The enzyme linked immuno sorbent assay (ELISA) kits (CRE)	Shanghai Jianglai Industrial Limited by Share Ltd	Cat: JL54862
BUN Detection Kit	Shanghai Jianglai Industrial Limited by Share Ltd	Cat: JL-T1014
Cell Counting Kit-8 (CCK-8)	Med Chem Express (Monmouth Junction, NJ, USA)	Cat: HY-K0301
Superoxide dismutase (SOD) assay kit	Solarbio Life Sciences	Cat: BC5165
Propidium iodide (PI) dye detection kit	Beyotime Biotechnology (Shanghai, China)	Cat: C1352M
Annexin V-FITC apoptosis detection kit	Beyotime Biotechnology (Shanghai, China)	Cat: C1062M
Comet assay kit	Beyotime Biotechnology (Shanghai, China)	Cat: C2041S
Experimental models: Cell lines		
L02	Fu Heng Biology	FH0109
MC38	Fu Heng Biology	FH0644
Experimental models: Organisms/strains		
BALB/c nude mice	Shanghai SLAC Laboratory Animal	Available upon request

(*Continued on next page*)

Continued

REAGENT or RESOURCE	SOURCE	IDENTIFIER
Software and algorithms		
Prism 9	GraphPad	https://www.graphpad.com
ImageJ	Schindelin et al.[51]	https://imagej.nih.gov/ij/
Other		
HT7700 Exalens TEM	Hitachi, Japan	https://www.hitachi-hightech.com/cn/zhcn/products/microscopes
Multimode 8 AFM	Bruker, Germany	https://www.bruker.com/zh/products-and-solutions/microscopes/materials-afm.html
UH4150 spectrophotometer	Hitachi, Japan	https://www.hitachi-hightech.com/cn/zhcn/products/analytical-systems/spectrophotometers/
Ultima IV 285 X-ray powder diffractometer XRD	Rigaku Co., Japan	https://rigaku.com/products/x-ray-diffraction-and-scattering
ESCALAB 250XI XPS	Thermo, USA	https://www.thermofisher.cn/cn/zh/home/industrial/spectroscopy-elemental-isotope-analysis.html
Malvern Zetasizer Nano ZS	Malvern, U.K.	https://www.malvernpanalytical.com.cn/products?view=product-ranges&display=grid&technologies=101953
Fluorescence spectrometer FLS980	Edinburgh Instruments, England	https://www.edinst.com/products/fluorescence-spectrometers
In-Vivo Master small animal NIR-II bioimaging system	Wuhan Grand-imaging Technology Co., Ltd	https://www.bio-equip.com/show1equip4379961.html
Confocal laser scanning microscope	Nikon A1+, Japan	https://www.microscope.healthcare.nikon.com/zh_CN/products/confocal-microscopes
InVision 128 MSOT system	iThera Medical, Germany	https://ithera-medical.com/products/preclinical-research/invision/
Cytoflex Flow Cell analyzer	Beckman Coulter	https://www.mybeckman.cn/flow-cytometry
High-performance liquid chromatography	Waters, MA, USA	https://www.waters.com/nextgen/cn/zh/products/chromatography.html

EXPERIMENTAL MODEL AND STUDY PARTICIPANT DETAILS

Cell culture

Mouse colon cancer cells (MC38) and human normal liver cells (L02) were respectively cultured in DMEM medium and RPMI 1640 medium containing 10% FBS and 1% penicillin/streptomycin. All cells were cultured at in sterile cell culture flasks at 37°C and 95% humidified atmosphere with 5% CO_2.

Animal model

All procedures and animal experiments were implemented in accordance with the requirements of the Institutional Animal Care and Use Committee of Fujian Medical University. BALB/c nude mice (female, 5–6 weeks old, ~20 g) were provided by Shanghai SLAC Laboratory Animal Co., Ltd. The animals were cared for following the guidelines for the care and use of laboratory animals in China. The mice were housed under specific-pathogen-free (SPF) controlled conditions of 22 ± 1°C and 60% ± 10% humidity with a 12 h light/dark cycle and free access to standard rodent diet and water for 1 week.

METHOD DETAILS

Synthesis

A 6.0 mg of $Cu(NO_3)_2{\cdot}3H_2O$ (0.085 mmol), 15.1 mg of ellagic acid (EA) (0.048 mmol), and 10 mg polyvinyl pyrrolidone (PVP) were dissolved in 10 mL of water. The pH value of mixing solution was adjusted to 9. Subsequently, the obtained mixture was ultrasonicated for 5 min, and stirred at room temperature for 10 min. Then, the mixture was added into an autoclave, and heated at 100°C for 12 h. After the autoclave was naturally cool to room temperature, the obtained product was purified by centrifugation at 8000 rpm for 10 min, washed with ethanol for three times to remove unreacted starting materials, and finally re-dispersed in water for further use.

In vitro H_2S-responsive behavior

In a typical experiment, NaHS solution (500 μL) with different concentrations (0, 0.4, 0.4, 0.8, 1.2, 1.6, and 3.0 mM) was added into Tris-HCl buffer (pH = 7.4, 500 μL) containing Cu/EA-MOF (0.5 mg mL^{-1}), respectively. The absorption spectra of obtained mixtures were tested by UV-Vis-NIR absorption spectrophotometer after incubation at room temperature for 10 min. Subsequently, PA imaging was conducted under excitation at 950 and 1280 nm.

In vitro drug release

In vitro EA release from Cu/EA-MOF was measured using a dialysis method under physiological and NaHS through HPLC. First, the Cu/EA-MOF solution containing 1 mg of EA was suspended in 2 mL of phosphate-buffered saline (PBS) with or without 1 mM NaHS and then transferred to respective dialysis membrane bags (molecular weight cutoff = 10,000 Da). Then, the bags were immersed into 50 mL centrifuge tubes containing 20 mL of PBS with or without 1 mM NaHS. The tubes were gently shaken at 37 °C at 110 rpm, 0.2 mL of aliquot was collected, and an equal volume of fresh corresponding PBS was replenished at predetermined time points. The amount of EA released was determined by HPLC.

Cell toxicity test

MC38 cells and L02 cells were selected to investigate the cell toxicity. Cells were seeded in 96-well culture plates (5×10^3 cells/well) for 12 h. Then, the cells were cultured in a medium containing different concentration (0–200 μg mL^{-1}) of Cu/EA-MOF for 24 h at 37°C. Following this, medium containing 10 μL CCK-8 solution was added to each well and the cells were incubated for 40 min. The absorption signal intensity at 450 nm of cells was recorded by ELISA instrument. Subsequently, the viability of cells was calculated by the following formula:

$$\text{Viability}\ (\%) = (\text{mean absorbance value of treatment group} / \text{mean absorbance value of control}) \times 100\%.$$

Evaluation of intercellular ROS

2′,7′-dichlorodihydrofluorescein diacetate (DCFH-DA) was selected as a fluorescent probe for the evaluation of ROS in cells, which can be oxidized and recover FL signal. S-adenosyl-L-methionine (SAM) was used to additionally enhance the endogenous levels of H_2S in MC38 cells. MC38 cells were seeded in 96-well plates and incubated for 12 h. Cells were divided into five groups:Control (PBS), EA, Cu/EA-MOF, Cu/EA-MOF + $ZnCl_2$, Cu/EA-MOF + SAM. Cells were pre-treated with PBS, $ZnCl_2$, or SAM for 1 h. Then the medium was removed and the cells were washed three times. Then, medium containing Cu/EA-MOF was added. The cells were incubated for 4 h before the Cu/EA-MOF medium was removed and replaced with a medium containing 20 μM DCFH-DA. Cells were cultured for 60 min in the dark. Finally, the FL images of cells were captured using CLSM with an excitation wavelength of 488 nm.

NIR-II FL and PA imaging of cells

MC38 cells ($\sim2\times10^4$) were seeded into a 96-wells plates and cultured overnight. All cells were divided into four groups: 1) control (Cu/EA/BBT-MOF), treated with PBS; 2) Cu/EA/BBT-MOF + $ZnCl_2$, treated with 300 μM $ZnCl_2$; 3) Cu/EA/BBT-MOF + SAM, treated with 200 μM SAM; and 4) Cu/EA/BBT-MOF + SAM + L-Cys, treated with 200 μM SAM +200 μM L-Cys. The MC38 cells were incubated with their respective treatments for 1 h. Additionally, the cells were incubated with Cu/EA/BBT-MOF for 12 h. Cells were collected, distributed in PBS, and stored in centrifuge tubes for imaging. NIR-II FL images were acquired using NIR-II FL imaging system equipped with an 808 nm excitation laser and a 1050 nm bandpass filter. The exposure time was 2000 ms. The NIR-II FL images of cell were further analyzed using the ImageJ software. The ratiometric PA images of tumors were captured under excitation at 950 and 1280 nm.

In vivo NIR-II FL and PA imaging of mice

To evaluate the biodistribution and response capability of Cu/EA/BBT-MOF *in vivo*, NIR-II FL and PA imaging was carried out. Cu/EA/BBT-MOF (200 μL, 1 mg mL^{-1}) was administered by intravenous injection. Aminooxyacetic acid (AOAA) (2 mg kg^{-1}) and SAM (20 mg kg^{-1}) were used for suppression and upregulation of endogenous H_2S, which were intraperitoneally administered 12 h before Cu/EA/BBT-MOFs injection. NIR-II FL images of MC38 tumor bearing mice at different time points were obtained at 1050 nm using an NIR-II FL imaging system with an 808 nm excitation laser (180 mW cm^{-2}). All mice were anesthetized by isoflurane. The exposure time was 500 ms, and a 1050 ± 50 nm band optical filter was selected. 12 h after administration, the mice were sacrificed. Major organs (heart, liver, spleen, lung, and kidney) and tumors were collected and imaged. NIR-II FL images and NIR-II FL signal intensity in the regions of interest were processed by ImageJ software. The ratiometric PA images of tumors were captured under excitation at 950 and 1280 nm.

Therapeutic efficiency *in vivo*

To study the synergistic anti-tumor therapy, MC38 cells (2×10^6) were implanted subcutaneously into female BALB/c-nude mice. All mice were divided into five groups: 1) PBS; 2) EA; 3) Cu/EA/BBT-MOFs; 4) Cu/EA/BBT-MOFs + AOAA, pre-treated with AOAA; and 5) Cu/EA/BBT-MOFs + SAM, pre-treated with SAM. Mice in the Cu/EA/BBT-MOF, Cu/EA/BBT-MOFs + AOAA, and Cu/EA/BBT-MOFs + SAM groups were injected with 2 mg mL^{-1} Cu/EA/BBT-MOF in a final volume of 100 μL. Mouse body weight, tumor

size, and mouse survival were recorded every 2 days. After 16 days of treatment, the mice were sacrificed. The tumors and major organs were collected for H&E, TUNEL, and immunofluorescent Ki67 staining.

QUANTIFICATION AND STATISTICAL ANALYSIS

All experimental data are presented as the means ± standard deviation (SD) of at least three independent experiments. Statistical analysis was conducted using Student's t-tests. Statistical significance is expressed as $^{*}p < 0.05$, $^{**}p < 0.01$, and $^{***}p < 0.001$.